Mesh Deformation Based on Fully Stressed Design: The Method and Two-Dimensional Examples

Su-Yuen Hsu[1] and Chau-Lyan Chang[2]

NASA Langley Research Center, Hampton, VA 23681

SUMMARY

Mesh deformation in response to redefined boundary geometry is a frequently encountered task in shape optimization and analysis of fluid-structure interaction. We propose a simple and concise method for deforming meshes defined with three-node triangular or four-node tetrahedral elements. The mesh deformation method is suitable for large boundary movement. The approach requires two consecutive linear elastic finite-element analyses of an isotropic continuum using a prescribed displacement at the mesh boundaries. The first analysis is performed with homogeneous elastic property and the second with inhomogeneous elastic property. The fully stressed design is employed with a vanishing Poisson's ratio and a proposed form of equivalent strain (modified Tresca equivalent strain) to calculate, from the strain result of the first analysis, the element-specific Young's modulus for the second analysis. The theoretical aspect of the proposed method, its convenient numerical implementation using a typical linear elastic finite-element code in conjunction with very minor extra coding for data processing, and results for examples of large deformation of two-dimensional meshes are presented in this paper.

KEY WORDS: Mesh deformation, shape optimization, fluid-structure interaction, fully stressed design, finite-element analysis, linear elasticity, strain failure, equivalent strain, Tresca failure criterion

INTRODUCTION

Mesh updating in response to redefined boundary geometry is a frequently encountered task in shape optimization and analysis of fluid-structure interaction. The updating can be accomplished by mesh deformation or mesh regeneration. In contrast to a regenerated mesh, a deformed mesh retains its original mesh connectivity. It is advantageous to retain mesh connectivity in shape optimization and analysis of fluid-structure interaction. Therefore, whenever mesh deformation is applicable, it is considered a preferred approach.

Gnoffo [1] and Nakahashi and Deiwert [2] employed a one-dimensional spring analogy to develop adaptive grid algorithms that may improve flowfield solutions. Subsequently, several researchers [3-7] applied the spring analogy to obtain deformed meshes that are consistent with moving boundaries. The progress was from use of only linear springs to inclusion of torsional springs, from uniform spring stiffness to variable spring stiffness, from ignoring coupling among displacement components to the standard structural formulation, and from two-dimensional (2-D) applications to 3-dimensional (3-D) applications. The very original spring-based method is simple and concise. However, without the aid of a strain tensor for multidimensional continuum, the best existing spring-based methods for 3-D applications do not have the advantage of simplicity or conciseness. A later advancement in mesh deformation techniques is the use of multidimensional linear elasticity analogy [8-12]. With the robust classical description of multidimensional continuum deformation, the elasticity-based methods yield more satisfactory results than the spring-based methods and can be formulated in a simple and concise manner.

In some other approaches, each displacement component of a mesh movement is governed by a partial differential equation, e.g., Laplacian equation [13, 14] and biharmonic equation [15]. Hence, there

[1] Research Engineer, Structural Mechanics and Concepts Branch
[2] Research Scientist, Computational Aerosciences Branch

is no coupling among the displacement components. Although theses approaches are simple and concise, their effectiveness is limited by the independence of the displacement components.

In the existing methods which employ variable stiffness (for the spring-based methods and elasticity-based methods) or variable diffusivity (for the Laplacian equation), the stiffness or diffusivity is assumed to be a function of measures of element (2-D or 3-D mesh cell) size (such as length, area, and volume) or quality (such as angle between two edges and Jacobian). For example, elements with initially smaller size or worse quality are assigned initially larger stiffness. However, smaller or worse elements do not necessarily undergo worse deformation (which is best described in terms of a strain tensor for a multidimensional continuum) when uniform stiffness is used. The existing methods may result in over-stiffening or under-stiffening of some elements, which has a negative impact on the effectiveness of mesh deformation. One may infer from the stiffness adjustment assumption that the existing methods tend to "assimilate" neighboring elements rather than tend to preserve the desirable original differences among the elements.

In this paper, we present a mesh deformation method which is analogous to the Fully Stressed Design (FSD), an elementary design method for linear elastic structures. The objective of the present approach is to "assimilate" deformation of neighboring elements (not elements themselves) and preserve the original differences in size and quality among mesh cells. Therefore, an analogue is to design a structure of which "all" the elements are stressed to an allowable equivalent strain when the structure is subjected to a boundary movement. Obviously, the FSD is a straightforward method to get a "quick" solution to the pseudo design problem. It is noted that any structural design process involves a material failure model in addition to the linear elastic stress-strain relation and equilibrium equation that the elasticity-based approaches require. For the present approach, the required failure model is a strain failure model that is defined in terms of an equivalent strain.

The present method is applicable to meshes defined with three-node triangular or four-node tetrahedral elements. The method requires two consecutive finite-element analyses of an isotropic continuum, using a prescribed displacement at the mesh boundaries to move the internal grid points. The first analysis is performed with homogeneous elastic property and the second with inhomogeneous elastic property. The FSD is employed to calculate, from the strain result of the first analysis, the element-specific Young's modulus for the second analysis. To this end, the Poisson's ratio of the elastic continuum is set to zero and a proposed form of equivalent strain (modified Tresca equivalent strain) is used. The formulation of the present method is simple and concise, its numerical implementation is convenient, and the method is effective in handling large boundary movement. Theses advantages are obvious in the following sections, where we present the theoretical aspect of the proposed method, its numerical implementation using a typical linear elastic finite-element code in conjunction with very minor extra coding for data processing, and results for examples of large deformation of 2-D meshes.

THEORETICAL ASPECT

Without loss of generality, we consider a meshed domain V as shown in Fig. 1. The boundary S consists of an inner boundary S_i and an outer boundary S_o. The mesh is expected to deform to a new one that has acceptable mesh quality and meets certain boundary displacement requirements, which define new boundary geometry. As in the elasticity-analogy approach, the original mesh is viewed as a finite-element mesh for an isotropic linear elastic material subject to the boundary displacement requirements of the mesh deformation problem and the desired deformed mesh is defined by a finite-element solution for the nodal displacement of the elasticity problem. A basic assumption of the proposed method is that all the inhomogeneous boundary conditions for the elasticity problem are of displacement type; namely, there is no inhomogeneous boundary condition of traction type.

If all the homogeneous boundary conditions are of displacement type as well, the volume average of the linear strain tensor depends on the displacement specified over the boundary but it is independent of the elastic property. This fact is obvious from the following derivation:

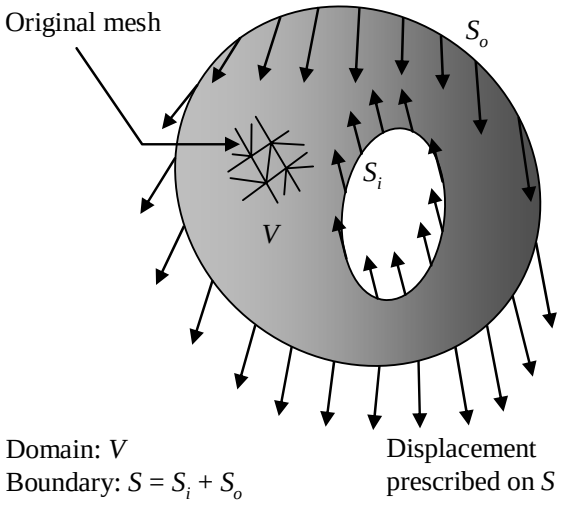

Figure 1. Schematic illustration of a linear elasticity problem with all the inhomogeneous boundary conditions of displacement type.

$$\frac{1}{V_0}\int_V \varepsilon_{ij} dv = \frac{1}{V_0}\int_V \frac{1}{2}\left(u_{i,j} + u_{j,i}\right) dv = \frac{1}{2V_0}\int_S (u_i n_j + u_j n_i) ds \tag{1}$$

where $i = 1,\ 2,\ \text{or},\ 3$, $j = 1,\ 2,\ \text{or},\ 3$, u_i and ε_{ij} are the Cartesian tensors of displacement and strain, respectively, V represents the domain occupied by the elastic continuum, S is the boundary of V, n_i is the outward unit vector normal to S, and V_0 is the volume of V. Because the average strain for a specific mesh deformation problem is fixed, a significant reduction in a strain concentration is usually accompanied by a strain increase in a low strain region.

In this paper, we primarily consider 2-D meshes defined with three-node triangular elements and 3-D meshes defined with four-node tetrahedral elements. The mesh deformation is accomplished by two consecutive linear finite-element analyses using the original mesh. The first one is performed with uniform elastic property to produce a baseline solution followed by the second one with non-uniform elastic property. The nodal displacements resulting from the second analysis define the desired new locations of the nodes. The fully stressed design is employed to determine suitable material stiffness for each element in order to have more uniform deformation. The FSD is typically applied to design of a structure whose primary response is governed by a linear constitutive relation between a scalar strain (or scalar generalized strain) and a scalar stress (or scalar generalized stress). For the case of a truss, the scalar linear relation is $\varepsilon = (1/K)P$, where ε and P are the axial strain and axial load in a rod of the truss, respectively, and $K = AE$ with A and E being the cross-sectional area of the rod and Young's modulus of the material of the rod, respectively. The FSD sizes the stiffness property of the aforementioned linear relation, so that the strain would be uniformly at its allowable value if the stress were not affected by the sizing. The FSD uses strain response calculated with assumed stiffness property values for an initial design to determine new stiffness property values for an improved design. For the case of a truss, the "FSD equation" used to calculate the improved stiffness of a rod is $K_{new} = (\varepsilon_{old}/\varepsilon_{allow})K_{old}$, where ε_{old} and K_{old} are the strain and stiffness of the rod of the initial design, respectively, ε_{allow} is the allowable strain, and K_{new} is the stiffness estimate for the improved design.

To apply the FSD to 2-D or 3-D isotropic continuum under multi-axial straining without ignoring any tensorial strain component in the calculation, some manipulation is necessary. First, we set the Poisson's ratio of the elastic continuum to zero. The setting reduces the stress-strain relation from

$$\begin{Bmatrix} \varepsilon_{11} \\ \varepsilon_{22} \\ \varepsilon_{33} \\ \varepsilon_{12} \\ \varepsilon_{23} \\ \varepsilon_{13} \end{Bmatrix} = \begin{bmatrix} \frac{1}{E} & \frac{-\nu}{E} & \frac{-\nu}{E} & 0 & 0 & 0 \\ \frac{-\nu}{E} & \frac{1}{E} & \frac{-\nu}{E} & 0 & 0 & 0 \\ \frac{-\nu}{E} & \frac{-\nu}{E} & \frac{1}{E} & 0 & 0 & 0 \\ 0 & 0 & 0 & \frac{1+\nu}{E} & 0 & 0 \\ 0 & 0 & 0 & 0 & \frac{1+\nu}{E} & 0 \\ 0 & 0 & 0 & 0 & 0 & \frac{1+\nu}{E} \end{bmatrix} \begin{Bmatrix} \sigma_{11} \\ \sigma_{22} \\ \sigma_{33} \\ \sigma_{12} \\ \sigma_{23} \\ \sigma_{13} \end{Bmatrix} \tag{2}$$

to

$$\varepsilon_{ij} = \frac{1}{E}\sigma_{ij} \tag{3}$$

where σ_{ij} is the Cartesian stress tensor. Note that the material compliance matrix is degenerated into a scalar and the material with the vanishing Poisson's ratio behaves as if it were a simple one-dimensional spring characterized by the same elastic constant for any type of loading. Secondly, an equivalent strain $F(\varepsilon_{ij})$, which is a nonnegative, homogeneous, and isotropic function of the strain components, is used as a scalar measure of the mesh deformation. Substituting Eq. 3 into $F(\varepsilon_{ij})$ and use of the functional homogeneity yield

$$F(\varepsilon_{ij}) = \frac{1}{E}F(\sigma_{ij}) \tag{4}$$

Equation 4 is analogous to the aforementioned linear constitutive relation for rods. By the analogy, the "FSD equation" used to calculate the improved material stiffness for an element is

$$E_{new} = \frac{F(\varepsilon_{ij}^{old})}{F_{allow}} E_{old} \tag{5}$$

where ε_{ij}^{old} is the element strain result of the first analysis, E_{old} and E_{new} are the Young's moduli used for the element for the first and second analyses, respectively, and F_{allow} is the targeted limit value of the equivalent strain. The two types of finite elements considered in this paper are the so-called constant-strain elements; there is no variation in ε_{ij}^{old} within each element. It should be noted that uniformly scaling up or down the Young's modulus affects the stress solution but does not affect the strain solution to the elasticity problems where all the inhomogeneous boundary conditions are of displacement type. For convenience, the numerical value of E_{old} (i.e., the uniform Young's modulus for the first analysis) is set to unity whatever unit of stress is chosen for the analysis.

Equation 5 cannot be employed directly to calculate E_{new} because E_{new} calculated with Eq. 5 for elements with a vanishing equivalent strain is zero and causes the singularity problem. Let F_{max} and F_{min} denote the maximum and minimum of the equivalent strain over all the elements that are not fully constrained by the boundary conditions, respectively. Note that $0 \le F_{min}$ because the equivalent strain is nonnegative. We only consider nontrivial problems, i.e., problems exhibiting a variation in strain;

therefore, $F_{min} < F_{max}$. We further restrict our investigation to problems for which the domains of analysis are sufficiently dominated by low-strain regions. We postulate that for these problems, F_{min} is a reasonable choice for the targeted strain level, if $0 < F_{min}$ and the maximum of E_{new} calculated with the FSD equation is not so much larger than the minimum as to cause the singularity problem. If $F_{min} = 0$ or $(F_{max}/F_{min})E_{old}$ is far too large to avoid the numerical problem, a numerically acceptable value should be chosen as the upper bound of the E_{new}/E_{old} ratio. It is a frequent observation that mesh deformation results for problems with a high F_{max}/F_{min} ratio is insensitive to the chosen upper bound of the E_{new}/E_{old} ratio provided that it is beyond a problem-dependent threshold. Guided by the above considerations, we propose the following equations to calculate the element-specific Young's modulus for the second analysis:

$$E_{new} = (1 + cT)E_{old} \tag{6}$$

$$T = \frac{F(\varepsilon_{ij}^{old}) - F_{min}}{F_{max} - F_{min}} \tag{7}$$

$$c = \begin{cases} (F_{max} - F_{min})/F_{min} & \text{if } (F_{max} - F_{min})/F_{min} \le c_{max} \\ c_{max} & \text{if } c_{max} \le (F_{max} - F_{min})/F_{min} \text{ or } F_{min} = 0 \end{cases} \tag{8}$$

where $E_{old} = 1$ with the unit of stress chosen for the analysis and $0 < c_{max}$ is the only numerical parameter. Equations 6 and 7 imply that elements with $F(\varepsilon_{ij}^{old}) = F_{min}$ are assigned the minimum of E_{new}, which is E_{old}, and elements with $F(\varepsilon_{ij}^{old}) = F_{max}$ are assigned the maximum, which is either $(F_{max}/F_{min})E_{old}$ or $(1 + c_{max})E_{old}$. The numerical parameter c_{max} should be set to as large a number as possible, subject to the condition that it should not render the finite-element equations prone to the singularity problem. Typically, c_{max} is not less than 10^3. It is straightforward to show that for the case of $(F_{max} - F_{min})/F_{min} \le c_{max}$, Eq. 6 is identical to the FSD equation with $F_{allow} = F_{min}$. For the case of $c_{max} \le (F_{max} - F_{min})/F_{min}$ or $F_{min} = 0$, it can be shown easily that the difference in E_{new} between Eq. 6 and the FSD equation with $F_{allow} = (F_{max} - F_{min})/c_{max}$ is negligible if $0.1 \le T \le 1$ and $10^3 \le c_{max}$. Equations 6-8 are modified FSD equations that are intended for the mesh deformation problems under present consideration.

The modified Tresca equivalent strain is proposed herein, which is nonnegative, homogeneous, and isotropic functions of the strain components. For 3-D cases, the modified Tresca equivalent strain is defined by

$$F_T(\varepsilon_{ij}) = Max\{r\varepsilon_I - \varepsilon_{III},\ e\varepsilon_I\} \tag{9}$$

For 2-D cases, it is defined by

$$F_T(\varepsilon_{ij}) = Max\{r\varepsilon_I - \varepsilon_{II},\ e\varepsilon_I\} \tag{10}$$

In the above, $\varepsilon_{III} \le \varepsilon_{II} \le \varepsilon_I$ are the principal strains, and $0 \le r < 1$ and $0 < e$ are numerical parameters. The $r\varepsilon_I - \varepsilon_{III}$ term of Eq. 9 and the $r\varepsilon_I - \varepsilon_{II}$ term of Eq. 10 account for failure due to combined maximum shear and contraction (or dilatation) on the principal planes, while the $e\varepsilon_I$ term accounts for maximum stretching failure. The development of the modified Tresca equivalent strain and its associated strain failure criterion, and the determination of the two parameters are presented in the Appendix. As

explained in the Appendix, reasonable values such as $r = 0.25$ and $e = 0.1$ can be chosen easily though heuristically. The present interest is to demonstrate that the above values, which are chosen with common engineering judgment, are good for a number of problems rather than that certain optimum values, which have to be determined by a sophisticated way, may produce the best result for a specific problem.

IMPLEMENTATION

The present method can be implemented with a basic finite-element code, which employs constant-strain elements, deals with isotropic linear elastic materials, allows use of element-specific elastic property, and calculates nodal displacements and element principal strains. Such a finite-element code is virtually ubiquitous. There is only one code that is specific to the present method and needs to be developed, and this code is rather short. For each element, the special code uses the principal strains from the first analysis to calculate the equivalent strain according to either Eq. 9 or Eq. 10 and then the element-specific Young's modulus according to Eqs. 6-8, and finally outputs the corresponding elastic material definition and its link to the element in preparation for the second analysis. If the chosen finite-element code allows an algebraic definition of the Young's modulus as a material function of some element-dependent field variables, e.g., element temperature, then an alternative is to have the special code only output the value of T (Eq. 7) and its associated element identity and directly define the material function (Eq. 6) in the analysis model. This alternative may considerably reduce the storage of the analysis model. A remark about the strain result of the first analysis is worth noting. Many finite-element codes or post-processors generate the so-called smoothed or averaged strain. The smoothed strain does not exactly represent element deformation. Therefore, the smoothed strain is not a good data source for the calculation of the element-specific Young's modulus. In fact, numerical findings have corroborated that the smoothed strain pronouncedly impairs the effectiveness of the present method.

The implementation of the proposed method simply consists of three steps: Step 1, performing the first round of finite-element analysis using $E_{old} = 1$ with the unit of stress chosen for the analysis; step 2, executing the above-mentioned special code to incorporate the element-specific E_{new} into the analysis model; step 3, performing the second round of finite-element analysis using the updated model. The nodal displacements resulting from the second analysis define the new nodal locations, which together with the unchanged mesh connectivity, define the deformed mesh.

In the present investigation, finite-element analysis is performed with the commercially available program NASTRAN Version 2005 of the MSC.Software Corporation. In addition, the required special code computes and outputs data of 2-D element temperature in a NASTRAN input format and an isotropic linear elastic material with the temperature-dependent Young's modulus is readily defined within a few lines in the NASTRAN input file for the second round of analysis. All computations for the numerical examples presented in the following sections are performed on a computer with an Intel Xeon 3.07 GHz CPU, 3 GB RAM, and the Linux operating system.

The parameters $r = 0.25$, $e = 0.1$, and $c_{max} = 10^6$ are used throughout the numerical examples presented in this paper. Using high-precision computing, NASTRAN should be able to handle the difference in element stiffness caused by $c_{max} = 10^6$ for any practical problem. As mentioned in the preceding section, we intend to evaluate the proposed method with a conveniently obtained single set of values of *r* and *e* for a variety of problems.

TWO-DIMENSIONAL EXAMPLE 1

We choose a numerical example reported in [15] as the first example in this paper. Shown in Fig. 2 is a 2-D mesh for a square domain whose edges are one unit long. Being similar to that used in [15], the mesh has 2048 elements and 1089 nodes. Both displacement components are set to zero at the lower edge

of the square. There is neither displacement in the *x* direction nor traction in the *y* direction at both the left and right edges. The *x* displacement at the upper edge is also set to zero. The only inhomogeneous boundary condition of this mesh deformation problem is a sinusoidal distribution of *y* displacement with an amplitude of 0.25 unit and a wave length of 1 unit enforced at the upper edge. The valley of the sinusoidal distribution is located at the midpoint of the upper edge. Each finite-element analysis for this example takes less than one second.

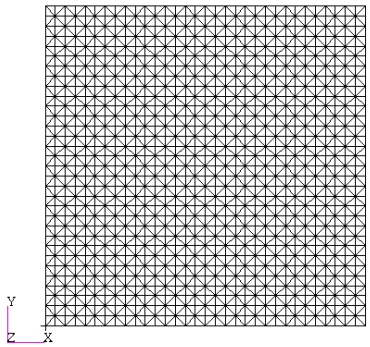

Figure 2. Undeformed mesh of the example 1.

The deformed mesh obtained from the first analysis is shown in Fig. 3. Although deterioration of the mesh is notable in Fig. 3, no grid line crossover has occurred. This suggests that the problem is still a mild one. However, the result obtained by solving Laplacian equations, reported in [15], indicates mesh penetration.

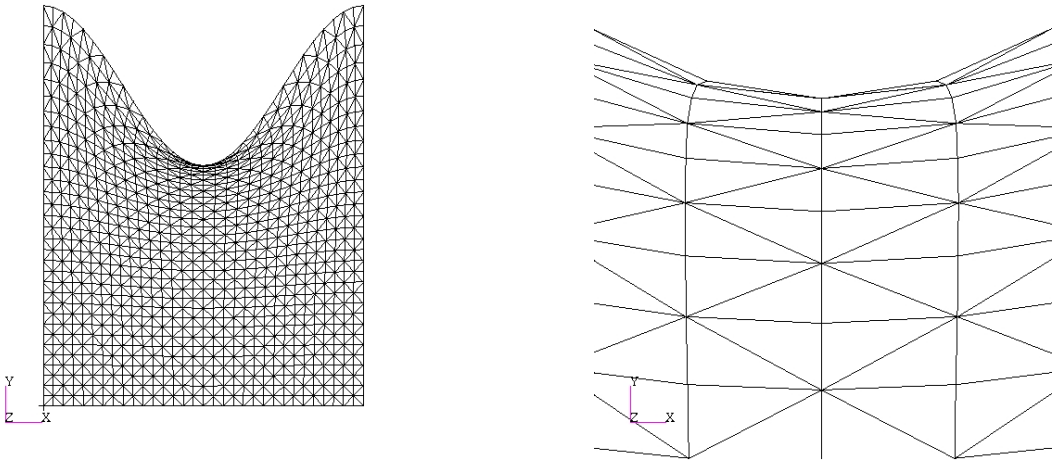

a) b)

Figure 3. Deformed mesh of the example 1, obtained from the first analysis: a) Entire mesh. b) Mesh around the midpoint of the upper edge.

The *c* value computed for the second analysis is $c = 3.044 \times 10^2$ and the mesh obtained from the second analysis is shown in Fig. 4. Obviously, the original mesh quality is well preserved after the

deformation. The result obtained by solving biharmonic equations, reported in [15], is similar to that shown in Fig. 4; however, the deformation is enforced in ten increments in [15].

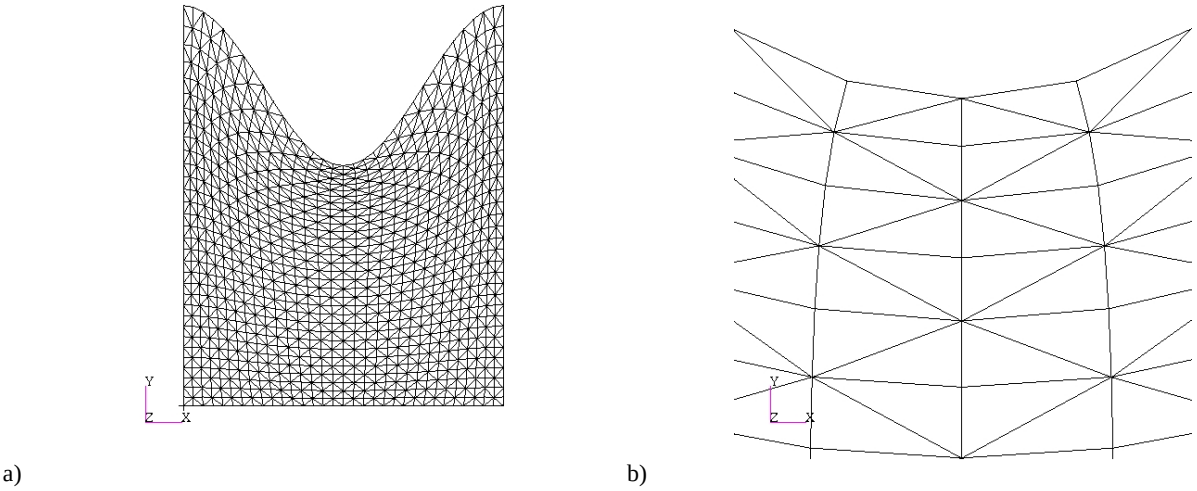

a) b)

Figure 4. Deformed mesh of the example 1, obtained from the second analysis: a) Entire mesh. b) Mesh around the midpoint of the upper edge.

TWO-DIMENSIONAL EXAMPLE 2

As shown in Fig. 5, a cylindrical object is stowed in a side bay. Three positions of the side-bay door are indicated in the figure. The door is slightly opened to the position A, opened to the halfway position B, and fully opened to the position C. The cylindrical object may be displaced to its ready position if the door is fully opened. The sub-domain, indicated in Fig. 5, with the cylindrical object stowed and the door in the position B is meshed, and the mesh is shown in Fig. 6, which has 353 elements and 211 nodes. Note that the thickness of the side-bay door is not modeled. Three cases of mesh deformation are investigated in this example: 1) mesh deformation due to door closing form the position B to the position A, 2) mesh deformation due to door opening from the position B to the position C; 3) mesh deformation due to door opening from the position B to the position C and the displacement of the cylindrical object from the stowage to the ready position. The external boundary is held stationary for each case.

The coarse mesh shown in Fig. 6, which may be called a “geometry mesh,” is supposed to represent the boundary geometry and boundary movement with sufficient accuracy and is intended to be deformed by the present method, but not to be used for actual engineering analysis (e.g., fluid dynamic computation). Another much finer mesh, which may be called an “analysis mesh,” should be used for the actual engineering analysis. Once the deformation of the geometry mesh is completed, most grid points of the analysis mesh can be relocated by interpolating the displacement field defined on the geometry mesh. By using a coarse geometry mesh, both computational time and strain concentration captured in finite-element analysis can be reduced; therefore, applicability of the mesh deformation method can be increased.

The deformed meshes obtained from the first analysis are shown in Figs. 7-9. The meshes are not usable because some elements around the free end of the door are crushed in all the three cases and several elements around the portion of the cylindrical boundary facing the door are also crushed in the first and third cases.

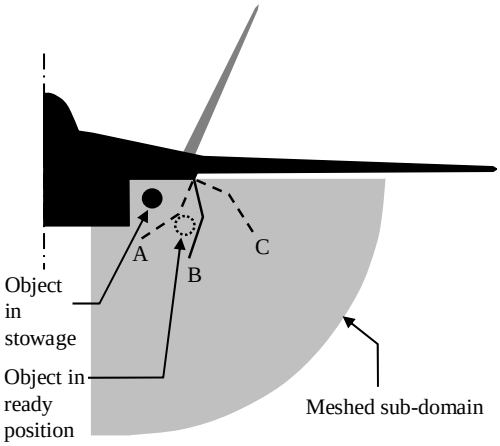

Figure 5. Problem definition of the example 2

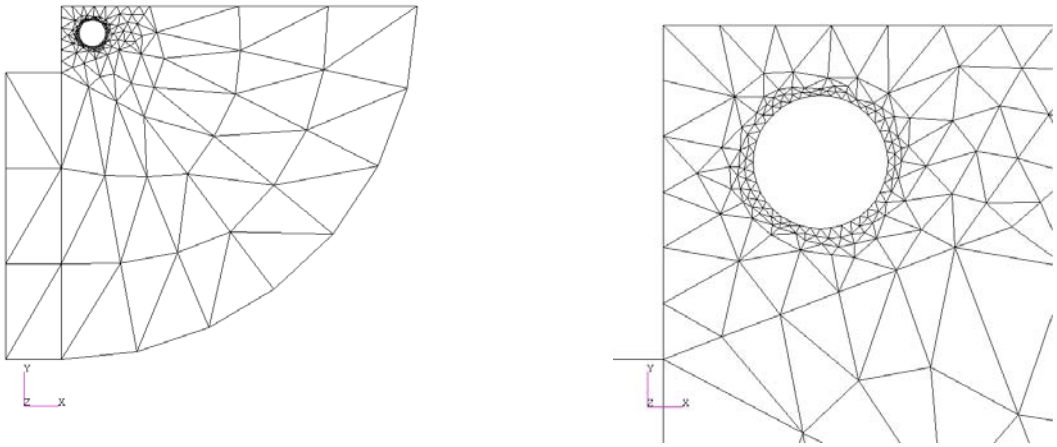

a) b)

Figure 6. Undeformed mesh of the example 2: a) Entire mesh. b) Mesh around the cylindrical object.

The respective c values computed for the second analysis for the three cases are $c = 1.307 \times 10^3$, $c = 7.549 \times 10^3$, and $c = 1.458 \times 10^2$, and the meshes obtained from the second analysis are shown in Figs. 10-12. It can be seen in the figures that the inhomogeneous elastic property computed by the proposed method conduces to far more uniform deformation and thus substantially improves the mesh quality. For example, comparing Fig. 9a with 12a Fig, one may see much more notable propagation of deformation toward the low strain regions due to the introduction of the property variation. No grid line crossover occurs in any of the deformed meshes obtained from the second analyses. Note that each of the three deformed meshes is derived from the same original mesh (Fig. 6) by using one increment. Therefore, a mesh for any intermediate instance during the process of changing the geometry, from the case 1 to the case 2 and through the case 3, can be conveniently derived from the same original mesh using one increment as well.

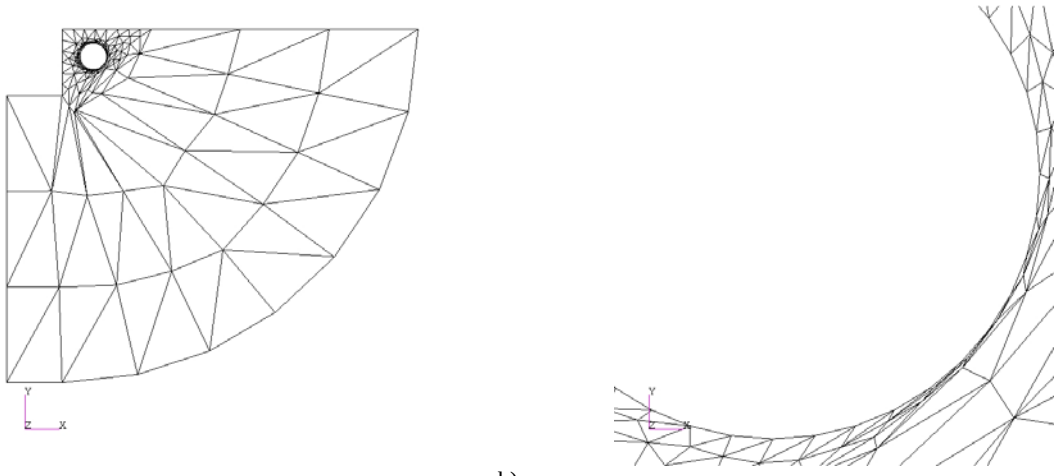

a) b)

Figure 7. Deformed mesh, door closing, the first analysis: a) Entire mesh. b) Mesh around the cylindrical object.

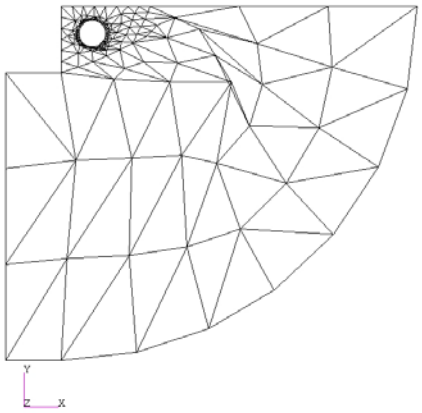

Figure 8. Deformed mesh, door opening, the first analysis.

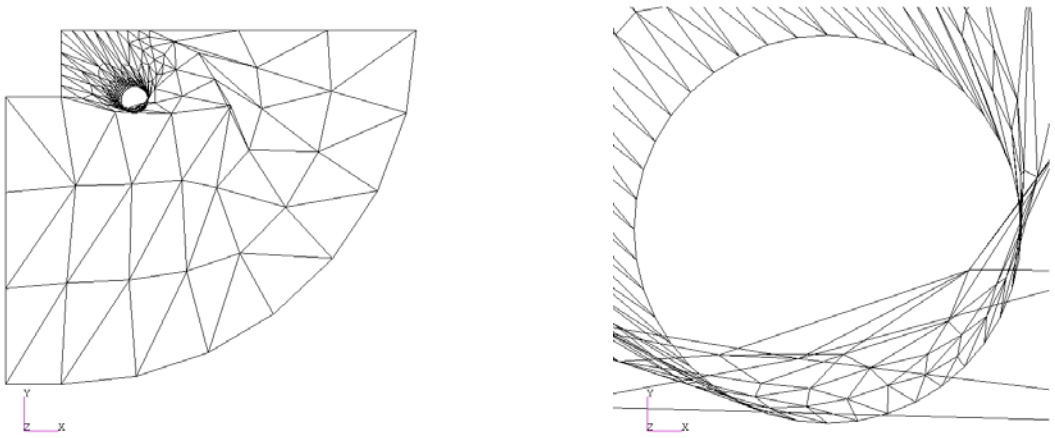

a) b)

Figure 9. Deformed mesh, door opening, the object displaced to the ready position, the first analysis: a) Entire mesh. b) Mesh around the cylindrical object.

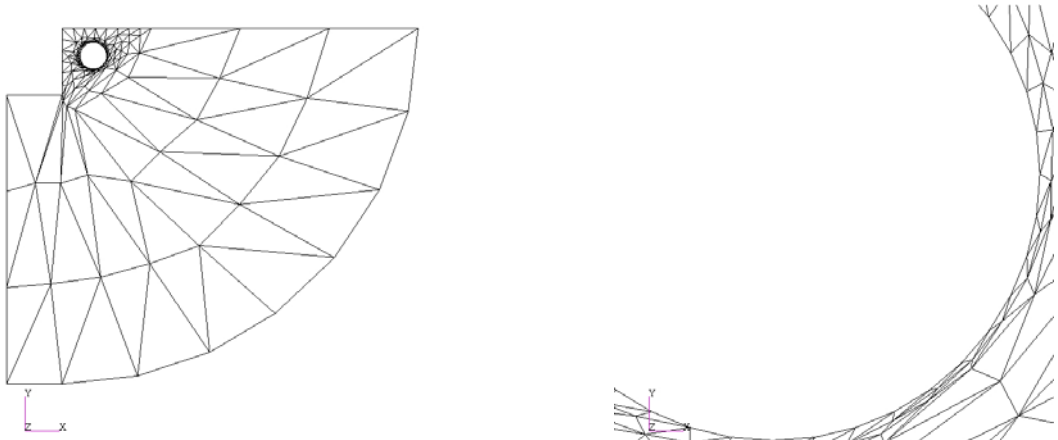

a) b)

Figure 10. Deformed mesh, door closing, the second analysis: a) Entire mesh. b) Mesh around the cylindrical object.

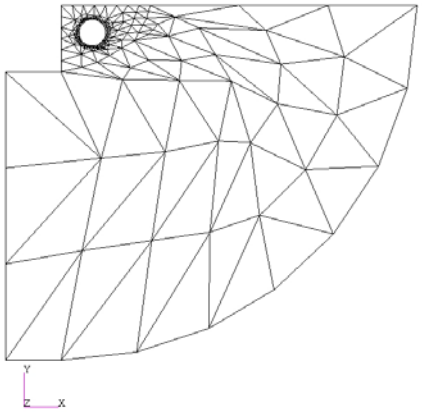

Figure 11. Deformed mesh, door opening, the second analysis.

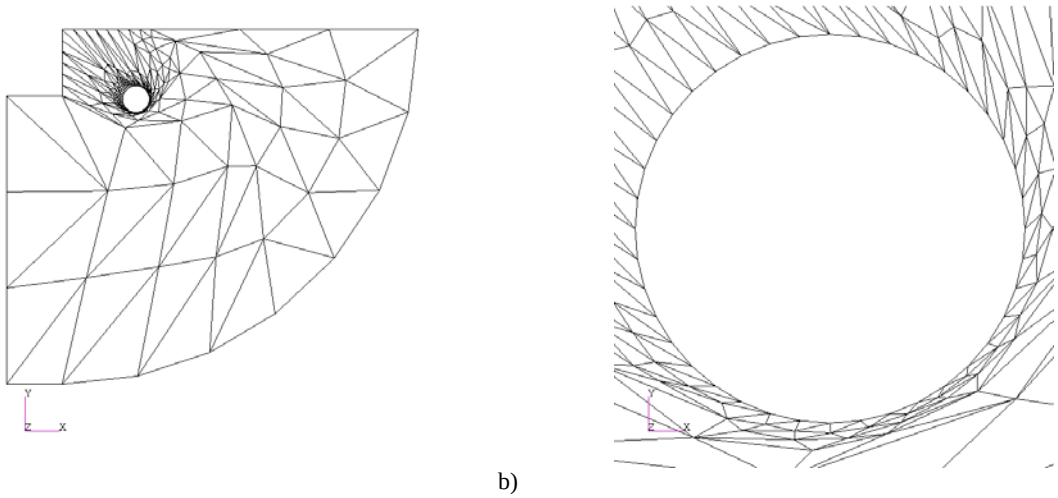

a) b)

Figure 12. Deformed mesh, door opening, the object displaced to the ready position, the second analysis: a) Entire mesh. b) Mesh around the cylindrical object.

TWO-DIMENSIONAL EXAMPLE 3

Shown in Fig. 13 is a 2-D unstructured mesh intended for a transonic flow over an airfoil. The mesh has a total of 18812 elements and 9598 nodes with many of them clustering near the airfoil surface. The chord of the airfoil is parallel with the *x*-axis and has a length of 1 unit. To demonstrate the effectiveness of the present method, we attempt to deform the mesh in four different ways: 1) by a translation of the airfoil by 0.5 unit in the flow (*x*) direction, 2) by a 0.5-unit upward (*y*) translation, 3) by a 45° rotation about the mid-chord point, and 4) by cambering the airfoil shape via imposing an arc-shaped distribution of upward (*y*) displacement (zero at both leading and trailing edges, and a peak displacement of 0.125 unit at the mid-chord point). The camber movement is often encountered in a design optimization process, while the rigid-body motion cases may appear in both design optimization and unsteady aerodynamic analysis. Each NASTRAN run takes about five seconds.

Figures 14-17 show the mesh patterns resulting from the first round of finite-element analysis. The uniform elastic property is employed at this stage and the resulting meshes are of very poor quality. It appears that the near-wall mesh points have been dragged along with the airfoil motion. In particular, grid line crossover occurs at the trailing edge for all the cases. Furthermore, the near-wall elements lose the quasi-orthogonality of the baseline mesh.

The respective c values computed for the second analysis for the four cases are $c = 6.922 \times 10^2$, $c = 7.009 \times 10^2$, $c = 4.156 \times 10^3$, and $c = 2.660 \times 10^4$, and the meshes obtained from the second analysis are shown in Figs. 18-21. Evidently, the artificial temperature fields created for the four test cases and the temperature-dependent elastic material have been effective in handling large boundary movement. The leading and trailing edges are problem-free and no grid line crossover is observed in the results. For the two translation cases, the orthogonality of the near-wall mesh is almost completely preserved. For the other two cases, the near-wall mesh, although less orthogonal than for the translation cases, still has good quality. The variable elastic property plays a crucial role in achieving the desirable mesh deformation. The impact of the property variation can be visualized, for example, by comparing Fig. 16a (invalid mesh) with Fig. 20a (valid mesh). It is seen from the comparison that the deformation is successfully propagated toward the low strain regions. A consequence of the propagation is the dramatic reduction in strain concentration, as indicated by Figs. 16b and 20b.

CONCLUDING REMARKS

We extend the idea of elasticity analogy to the idea of FSD analogy. We set the Poisson's ratio to zero in order to retain all the strain components in the FSD formulation and thus obtain the formulation suitable for general mesh deformation problems. The strain failure model based on the modified Tresca equivalent strain, which we propose specifically to characterize mesh deformation, is used as the failure criterion required by the FSD. The entire formulation of the method is concise and can be conveniently implemented by using a typical linear elastic finite element code. The application of the method to the various large deformations of the 2-D meshes is demonstrated, where consistently satisfactory mesh quality is obtained by using the conveniently obtained single set of values of the numerical parameters, i.e., $r = 0.25$ and $e = 0.1$. In contrast, the existing methods from the literature exhibit difficulties in solving similar problems.

The present method may be easily adapted to 2-D meshes containing four-node quadrilateral elements and 3-D meshes containing eight-node hexahedral elements. Because generally, strain distribution in such elements is not constant, the equivalent strain needs to be evaluated by using the actual strain at each corner of each element and then the maximum equivalent strain for the element is determined. The maximum equivalent strain for each element should be used as $F(\varepsilon_{ij}^{old})$ for the element in the above formulation of the proposed mesh deformation method; otherwise, the formulation remains the same.

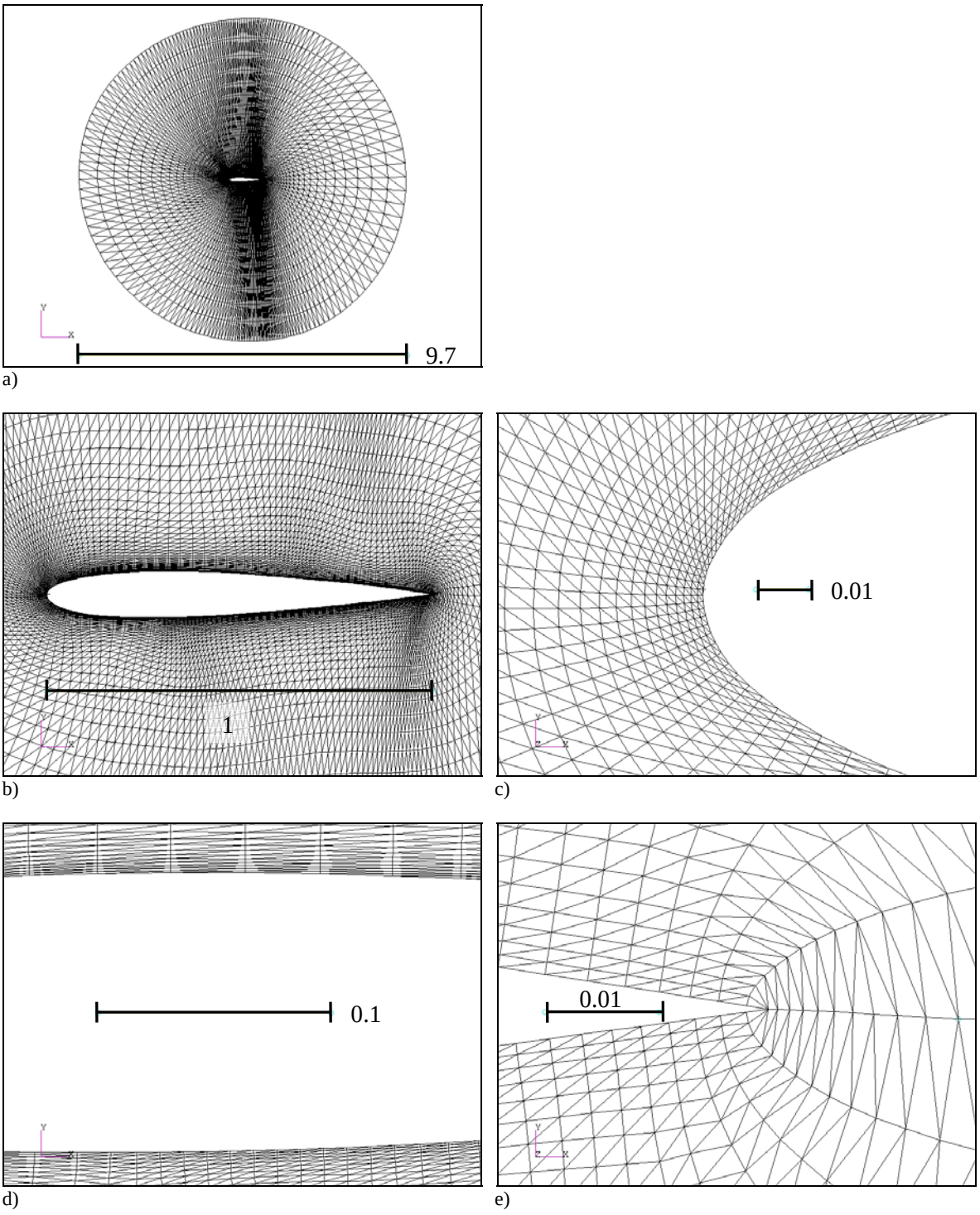

Figure 13. Undeformed mesh of the example 3: a) Entire mesh. b) Mesh around the airfoil. c) Mesh around the leading edge. d) Mesh around the mid chord. e) Mesh around the trailing edge.

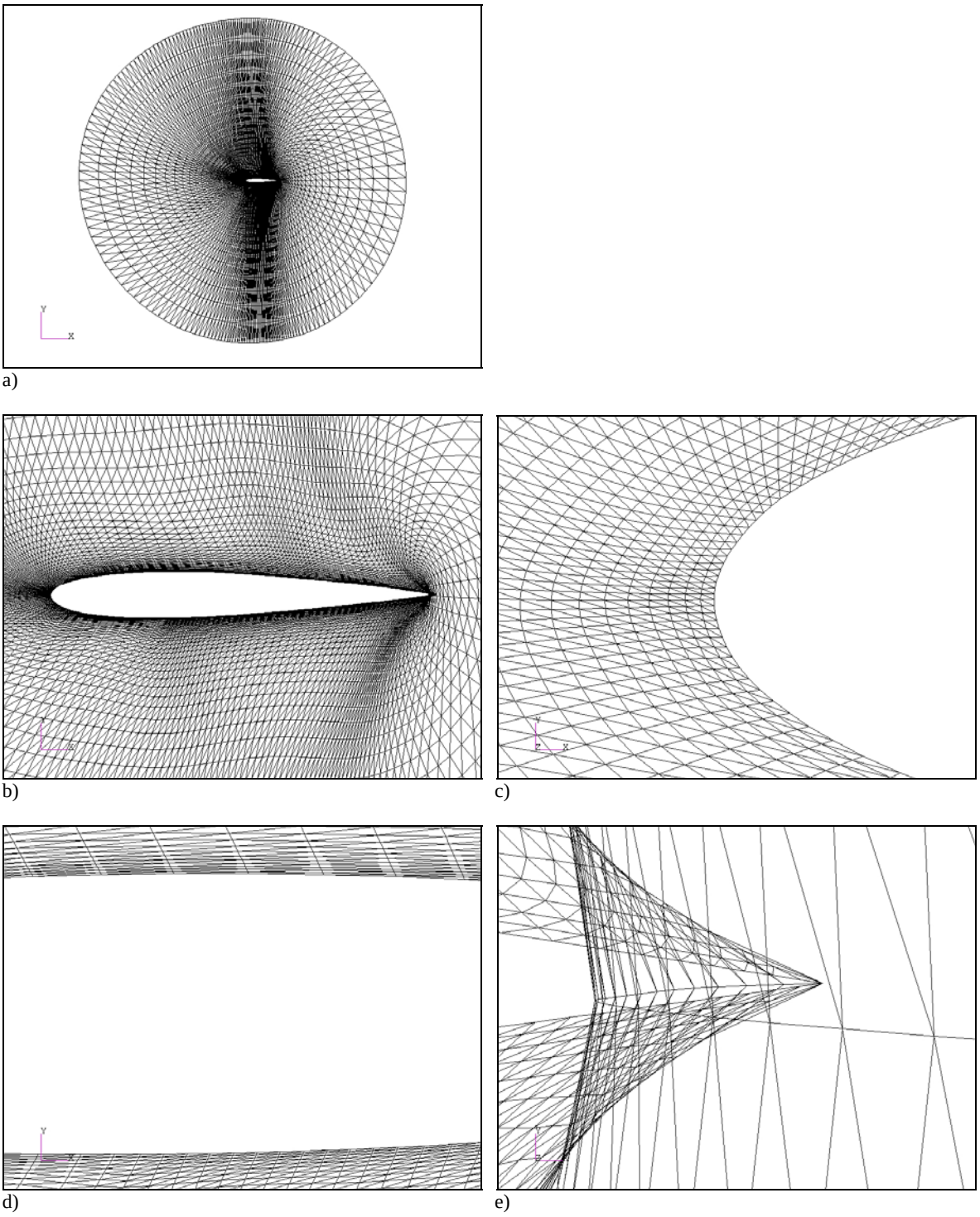

Figure 14. Mesh deformed by a 0.5-unit translation of the airfoil in the flow (x) direction, obtained from the first analysis: a) Entire mesh. b) Mesh around the airfoil. c) Mesh around the leading edge. d) Mesh around the mid chord. e) Mesh around the trailing edge.

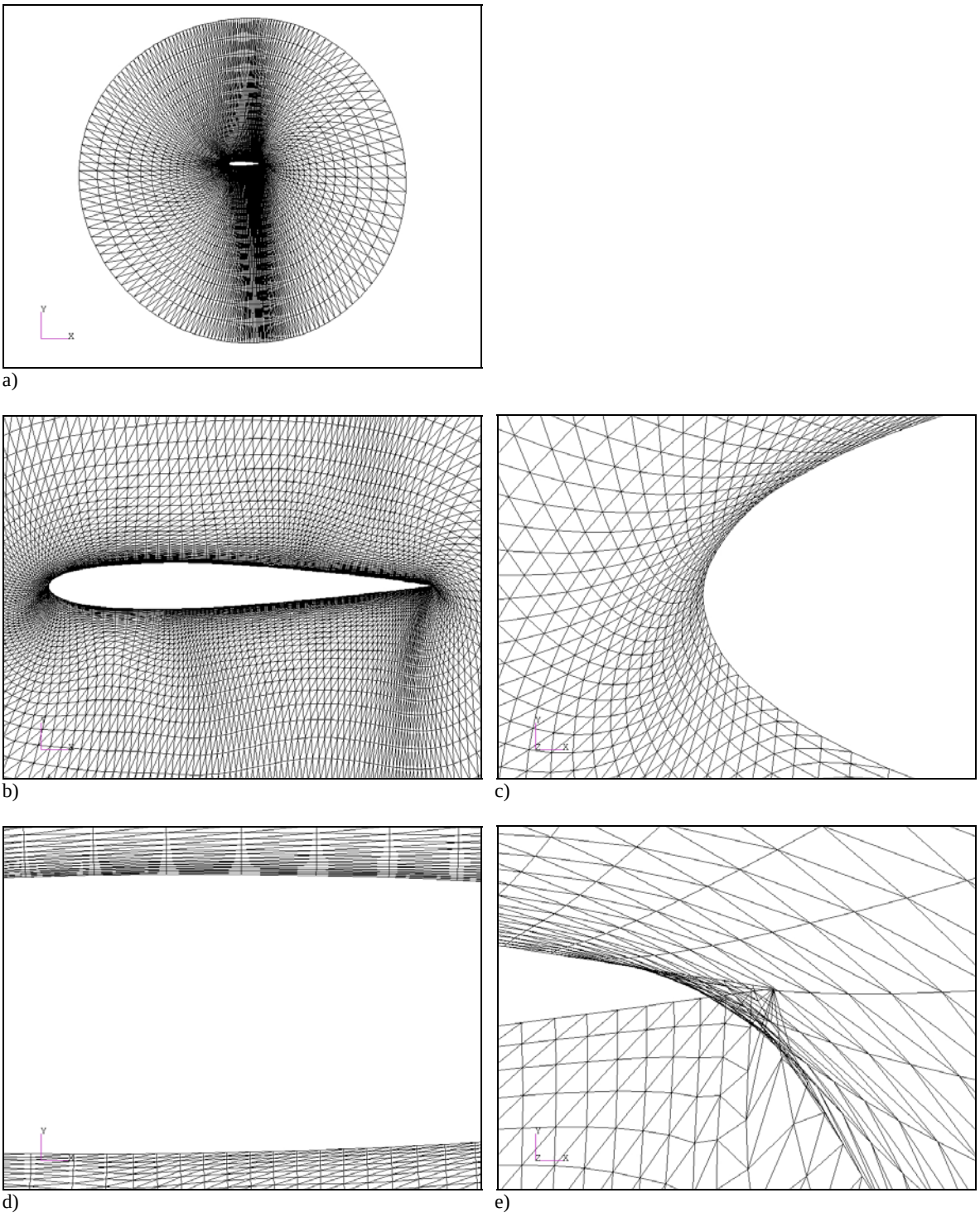

Figure 15. Mesh deformed by a 0.5-unit upward (*y*) translation of the airfoil, obtained from the first analysis: a) Entire mesh. b) Mesh around the airfoil. c) Mesh around the leading edge. d) Mesh around the mid chord. e) Mesh around the trailing edge.

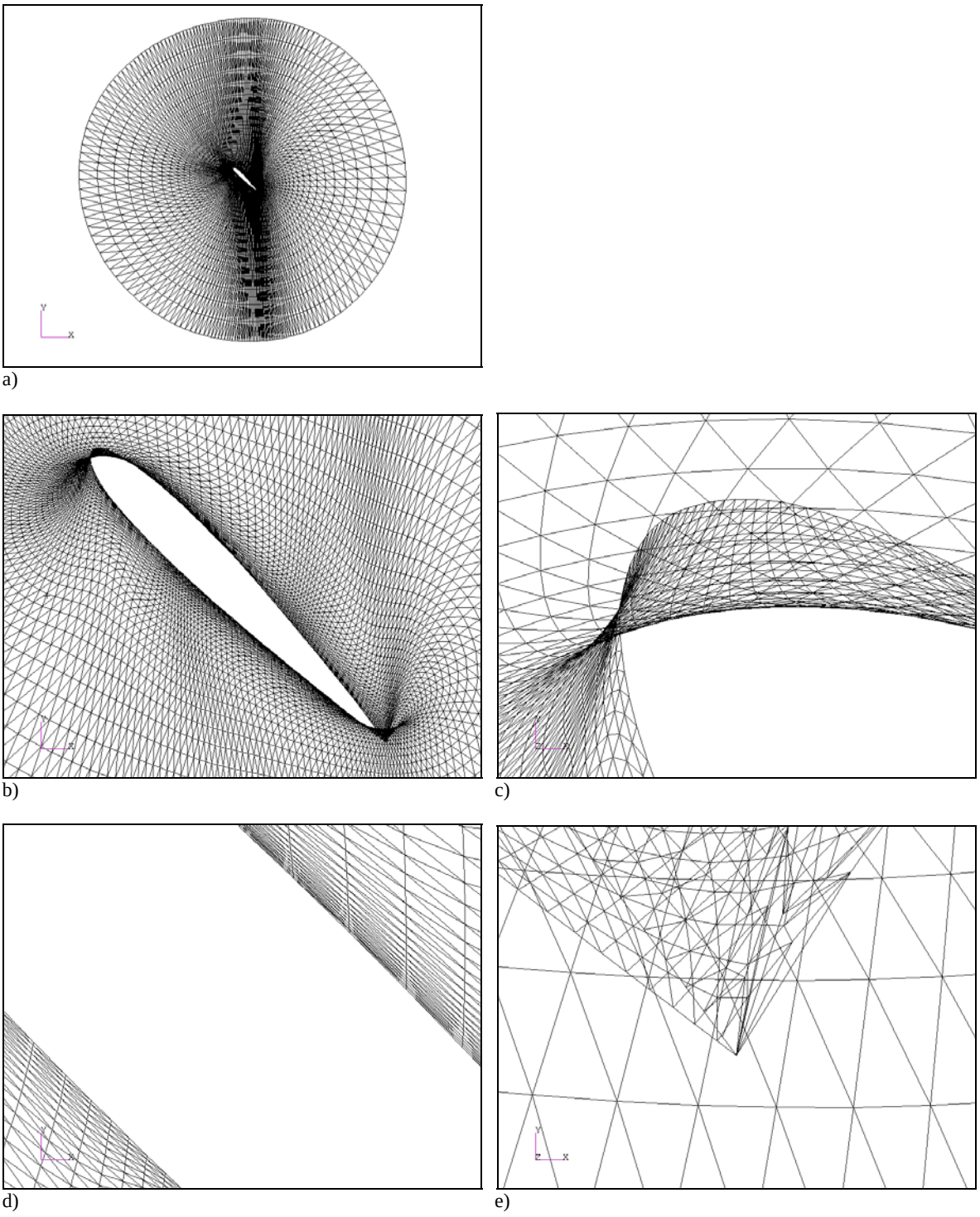

Figure 16. Mesh deformed by a 45° rotation of the airfoil about the mid-chord point, obtained from the first analysis: a) Entire mesh. b) Mesh around the airfoil. c) Mesh around the leading edge. d) Mesh around the mid chord. e) Mesh around the trailing edge.

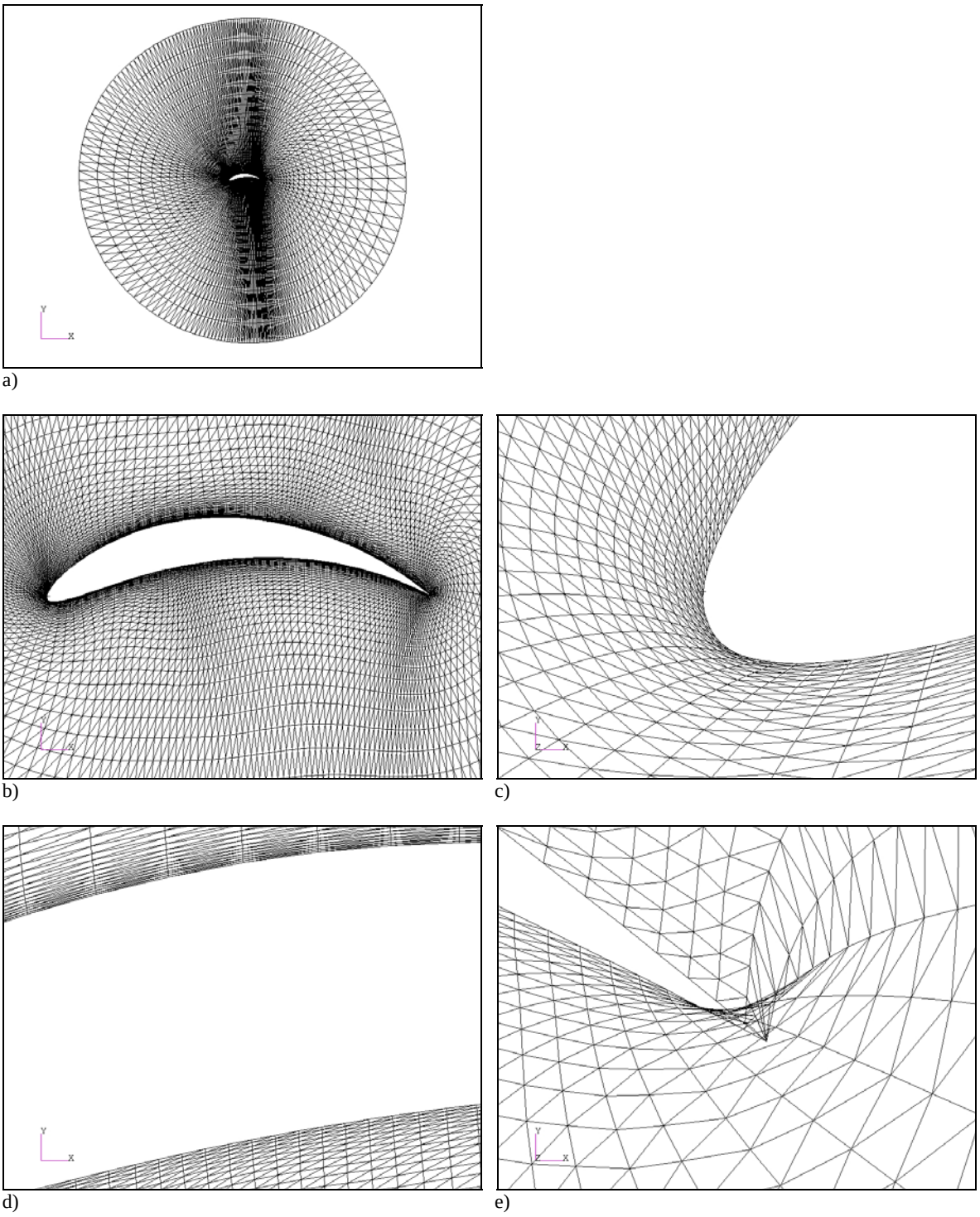

Figure 17. Mesh deformed by cambering the airfoil shape, obtained from the first analysis: a) Entire mesh. b) Mesh around the airfoil. c) Mesh around the leading edge. d) Mesh around the mid chord. e) Mesh around the trailing edge.

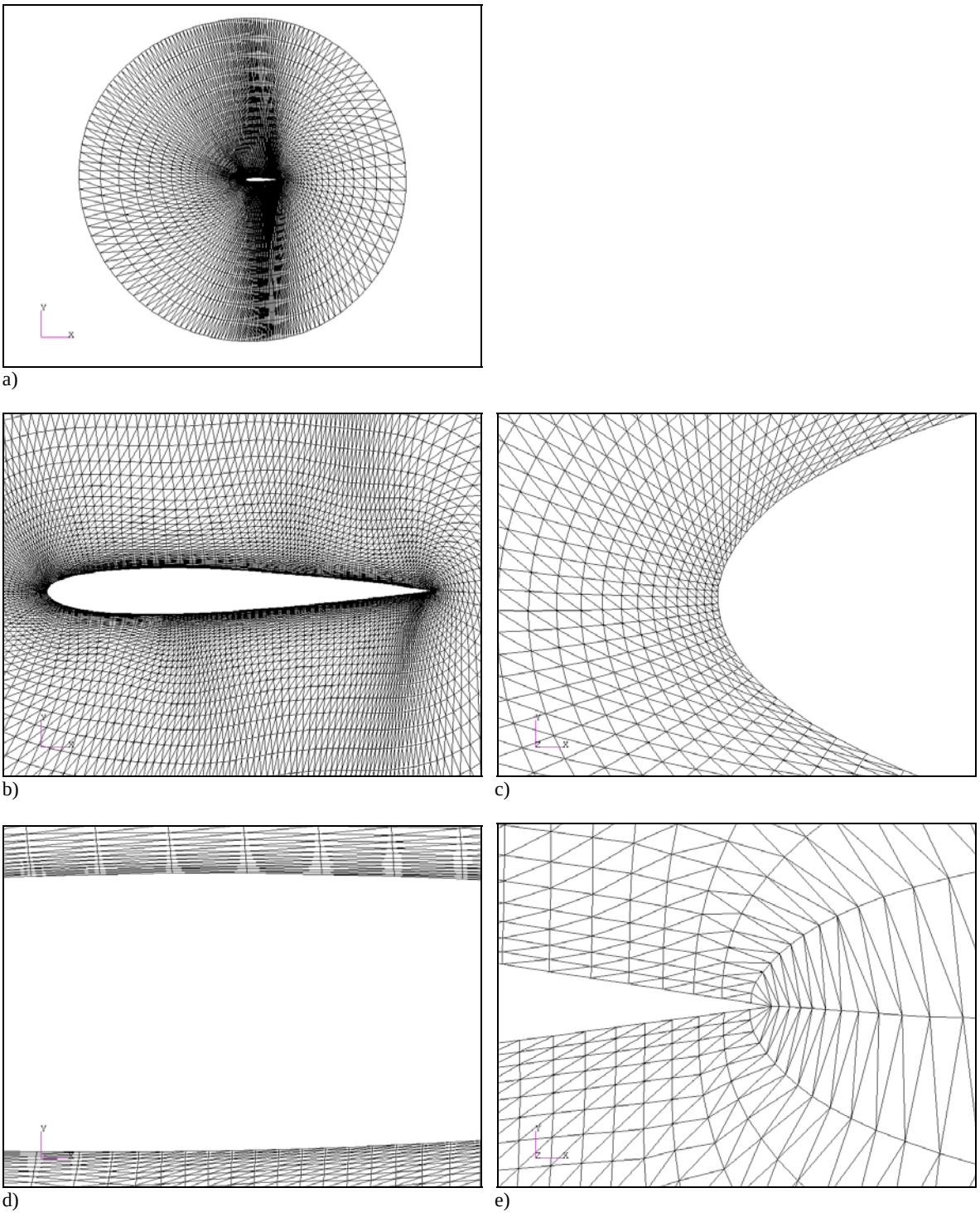

Figure 18. Mesh deformed by 0.5-unit translation of the airfoil in the flow (x) direction, obtained from the second analysis: a) Entire mesh. b) Mesh around the airfoil. c) Mesh around the leading edge. d) Mesh around the mid chord. e) Mesh around the trailing edge.

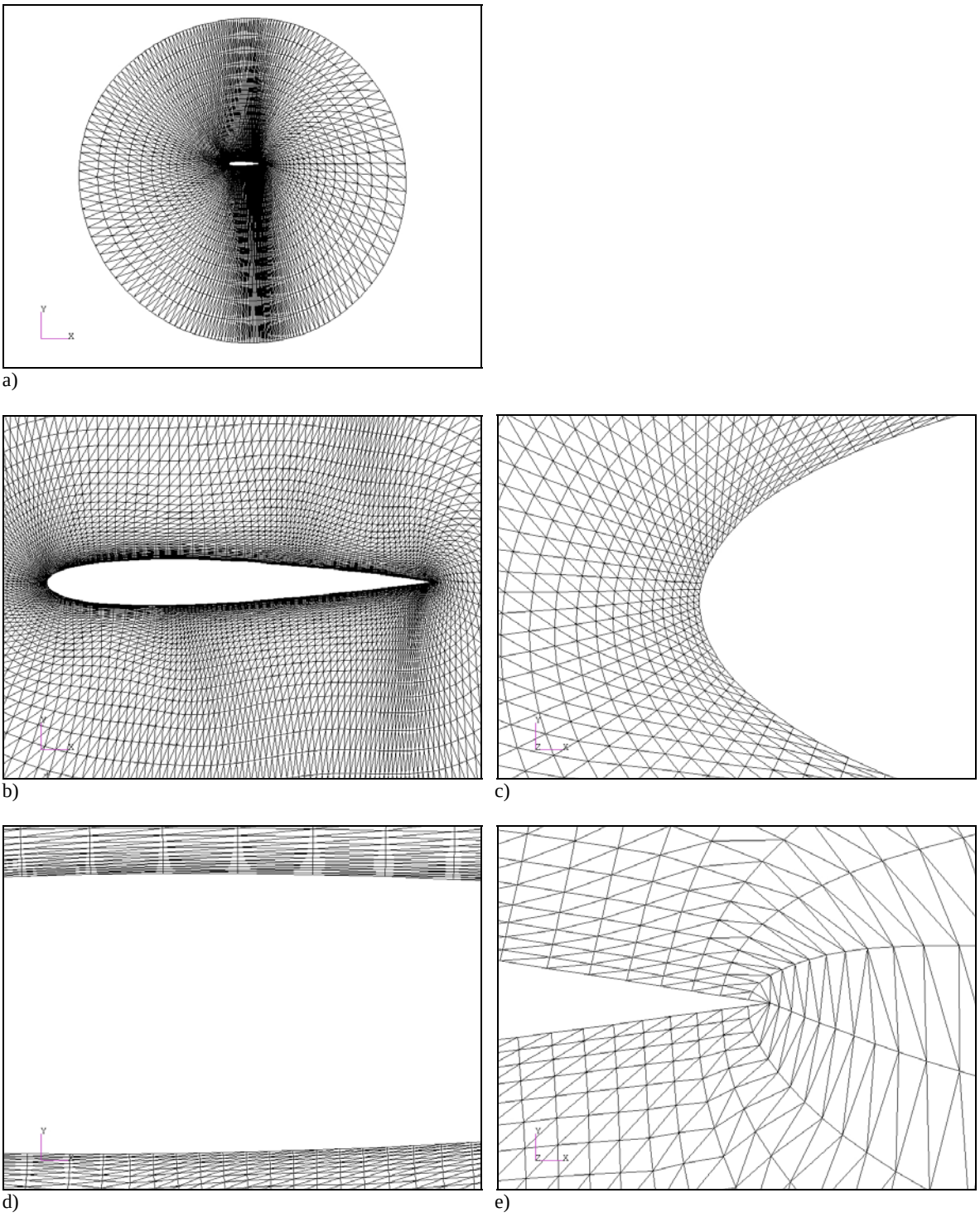

Figure 19. Mesh deformed by a 0.5-unit upward (*y*) translation of the airfoil, obtained from the second analysis: a) Entire mesh. b) Mesh around the airfoil. c) Mesh around the leading edge. d) Mesh around the mid chord. e) Mesh around the trailing edge.

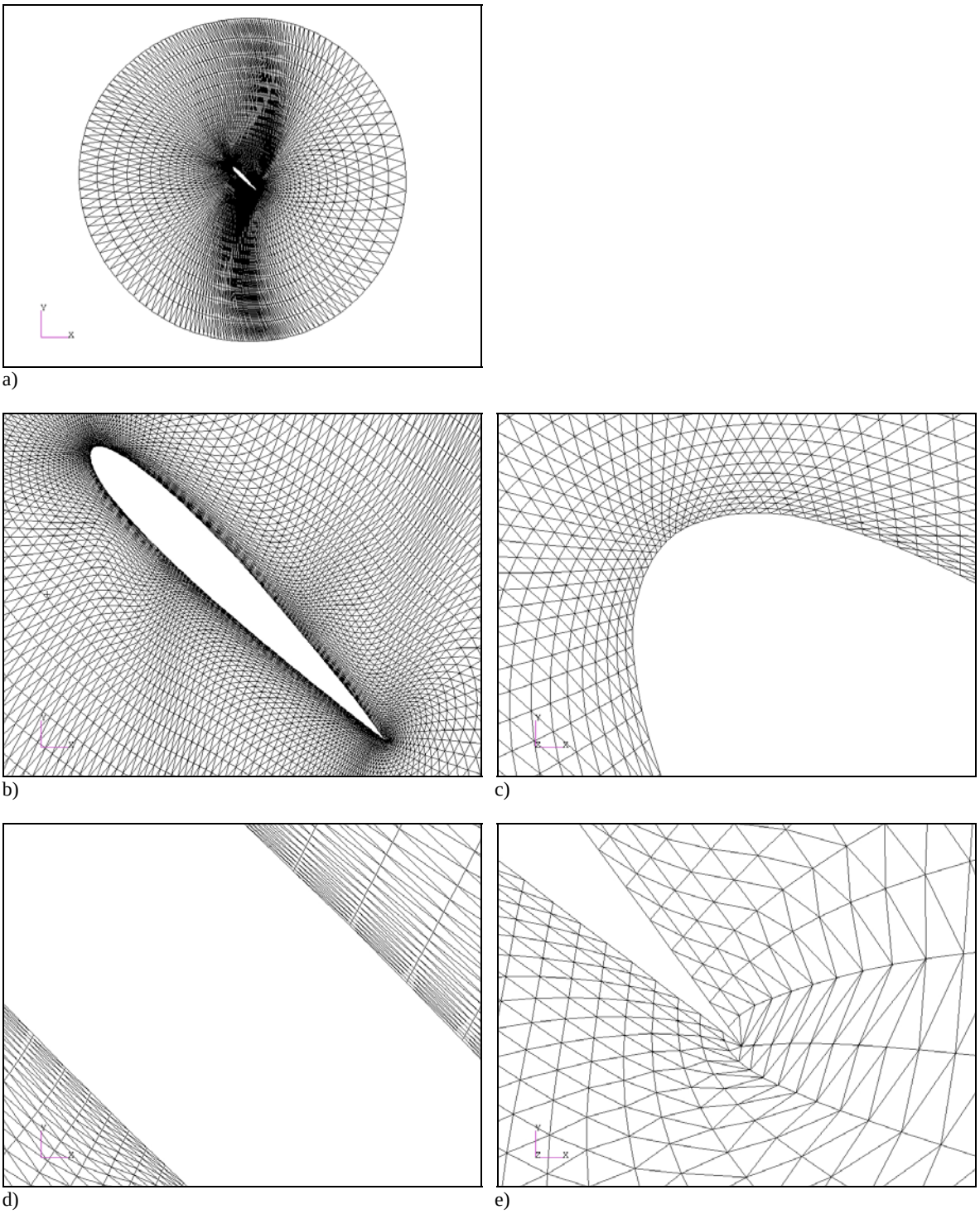

Figure 20. Mesh deformed by 45° rotation of the airfoil about the mid-chord point, obtained from the second analysis: a) Entire mesh. b) Mesh around the airfoil. c) Mesh around the leading edge. d) Mesh around the mid chord. e) Mesh around the trailing edge.

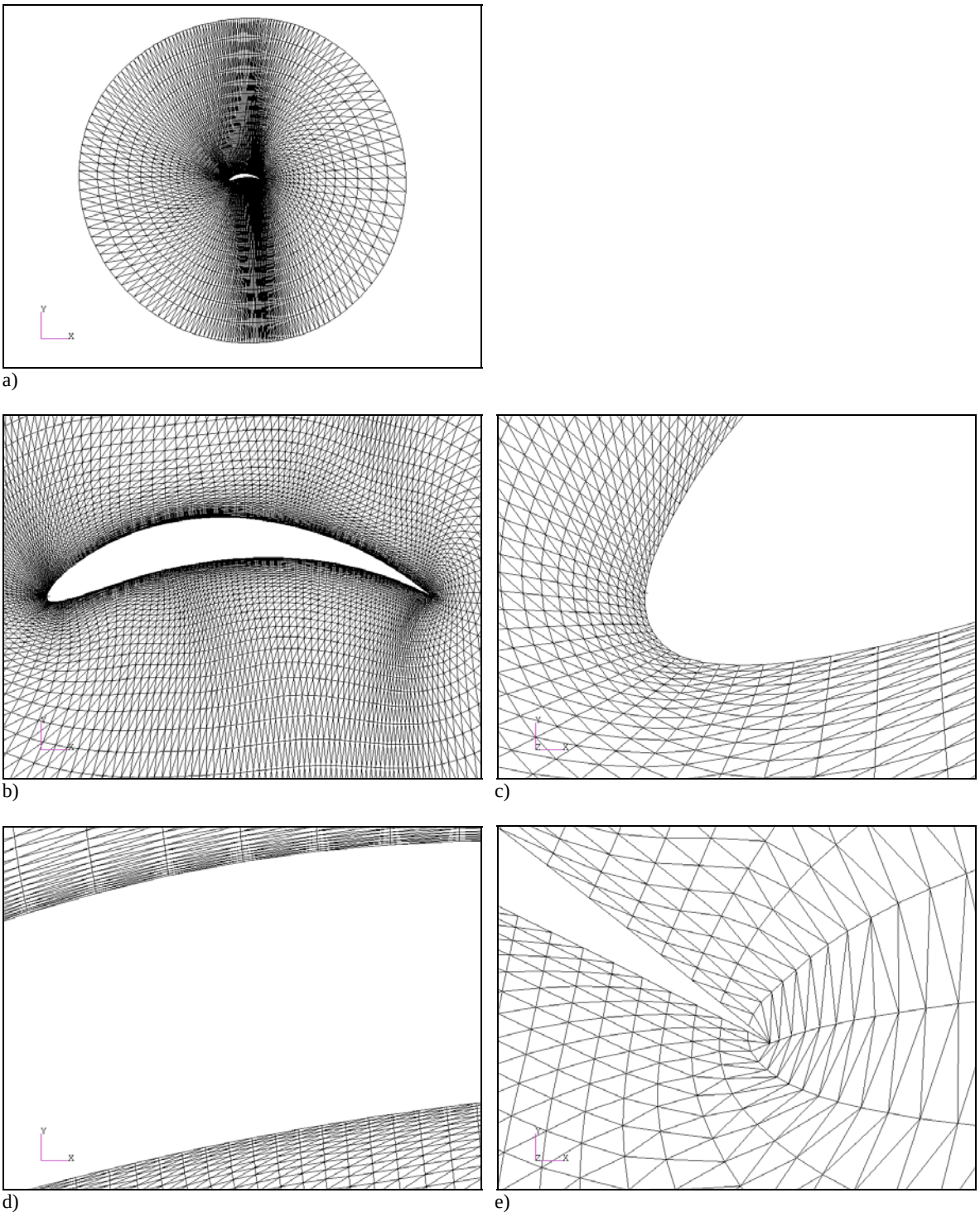

Figure 21. Mesh deformed by cambering the airfoil shape, obtained from the second analysis: a) Entire mesh. b) Mesh around the airfoil. c) Mesh around the leading edge. d) Mesh around the mid chord. e) Mesh around the trailing edge.

Numerical efficiency is critical if the present method is applied to large 3-D meshes, in particular, 3-D meshes for viscous fluid dynamic analysis. A way to shorten computational time is to deform a coarse geometry mesh first, then map "off-boundary nodes" of a fine analysis mesh to the deformed state, and finally perform deformation of a boundary layer of the analysis mesh to displace "near-boundary nodes" (i.e., nodes inside the boundary layer). The near-boundary nodes are those that may not be accurately relocated by the mapping. To ensure that the number of the near-boundary nodes is acceptably small, boundary geometry and boundary movement need to be modeled with the geometry mesh sufficiently accurately. To achieve the accuracy and keep the number of degrees of freedom of the geometry mesh small at the same time, degenerated higher-ordered elements of which all the non-corner nodes are placed on the boundary of the geometry mesh may be used. Besides the time saving, weaker strain concentration is captured in finite-element analysis due to the coarseness of the geometry mesh. Results of implementation of 3-D geometry meshes will be reported in a sequel.

REFERENCES

1. Gnoffo, P. A., A Finite-Volume Adaptive Grid Algorithm Applied to Planetary Entry Flowfields, AIAA J., 21, 1983, pp. 1249–1254.
2. Nakahashi, K. and Deiwert, G. S., Self-Adaptive-Grid Method with Application to Airfoil Flow, AIAA J., 25, 1987, pp. 513–520.
3. Batina, J. T., Unsteady Euler Airfoil Solutions Using Unstructured Dynamic Meshes, AIAA J., 28, 1990, pp. 1381–1388.
4. Farhat, C., Degand, C., Koobus, B., and Lesoinne, M., Torsional Springs for Two-Dimensional Dynamic Unstructured Fluid Meshes, Comput. Methods Appl. Mech. Engrg., 163, 1998, pp. 231–245.
5. Murayama, M., Nakahashi, K., and Matsushima, K., Unstructured Dynamic Mesh for Large Grid Movement and Deformation, AIAA Paper 2002-0122, 2002.
6. Degand, C. and Farhat, C., A Three-Dimensional Torsional Spring Analogy Method for Unstructured Dynamic Meshes, Comput. Struct., 80, 2002, pp. 305-316.
7. Burg, C. O. E., A Robust Unstructured Grid Movement Strategy Using Three-Dimensional Torsional Springs, AIAA Paper 2004-2529, 2004.
8. Tezduyar, T. E. and Behr, M., A New Strategy for Finite-Element Computations Involving Moving Boundaries and Interfaces- the Deforming-Spatial-Domain/Space-Time Procedure: I. the Concept and the Preliminary Numerical Tests, Comput. Methods Appl. Mech. Engrg., 94, 1992, pp. 339–351.
9. Johnson, A. A. and Tezduyar, T. E., Simulation of Multiple Spheres Falling in a Liquid-Filled Tube, Comput. Methods Appl. Mech. Engrg., 134, 1996, pp. 351-373.
10. Cavallo, P. A., Hosangadi, A., Lee, T. A., and Dash, S. M., Dynamic Unstructured Grid Methodology with Application to Aero/Propulsive Flowfields, AIAA Paper 97-2310, 1997.
11. Nielsen, E. J. and Anderson, W. K., Recent Improvements in Aerodynamic Design Optimization on Unstructured Meshes, AIAA J., 40, 2002, pp. 1155–1163.
12. Stein, K., Tezduyar, T., and Benney, R., Mesh Moving Techniques for Fluid-Structure Interactions with Large Displacements, J. Appl. Mech., 70, 2003, pp. 58-63.
13. Masud, A. and Hughes, T. J. R., A Space-Time Finite Element Method for Fluid-Structure Interaction, SUDAM Report No. 93-3, Stanford Univ., Stanford, CA, 1993.
14. Crumpton, P. I. and Giles, M. B., Implicit Time-Accurate Solutions on Unstructured Dynamic Grids, Int. J. Numer. Methods Fluids, 25, 1997, pp. 1285–1300.
15. Helenbrook, B. T., Mesh Deformation Using the Biharmonic Operator, Int. J. Numer. Methods Engrg., 56, 2003, pp. 1007-1021.

APPENDIX

In the existent methods of elasticity analogy or spring analogy, mesh deformation is calculated by structural analysis. All the existent methods are based on the equation of equilibrium and certain stress-strain relations. However, none of the existent method has employed the concept of material failure, which is an essential element of classical structural analysis.

A strain failure criterion can be set up to determine whether a mesh cell is so severely deformed that it cannot be used for computation. Typically, a strain failure criterion is a nonnegative and homogeneous function of the strain tensor. Such a failure criterion can be cast into a simple statement that a material fails when an equivalent strain reaches an allowable value.

We borrow the notion of the Tresca equivalent stress to define a Tresca equivalent strain as the following:

$$F_T^0(\varepsilon_{ij}) = Max\left\{\left|\varepsilon_I - \varepsilon_{II}\right|,\ \left|\varepsilon_{II} - \varepsilon_{III}\right|,\ \left|\varepsilon_{III} - \varepsilon_I\right|\right\} \tag{A1}$$

where ε_I, ε_{II}, and ε_{III} are the principal strains. The strain failure criterion associated with F_T^0 is "A material fails if $F_T^0 \geq \varepsilon_C^f$, where $0 < \varepsilon_C^f \leq 100\%$ is a material parameter, magnitude of the uniaxial compressive failure strain." Obviously, F_T^0 is a nonnegative, homogeneous, and isotropic function of the strain tensor. The failure surface represented by $F_T^0(\varepsilon_{ij}) = \varepsilon_C^f$ is an open-ended hexagonal cylinder with the centerline defined by $\varepsilon_I = \varepsilon_{II} = \varepsilon_{III}$ in the principal strain space. Note that the Tresca equivalent strain is a direct measure of the maximum shear strain, and it is independent of the hydrostatic strain component. These are desirable features because it is shear deformation of a mesh cell (not volumetric deformation) that accounts for primary deterioration of the mesh cell. However, deterioration of mesh quality is not exactly independent of the volumetric deformation. For example, an initially perfect mesh cell (say, an equilateral triangle for the 2-D case) may expand or contract to an unacceptable size without any change in the aspect ratio or twist.

For brevity but without loosing generality, we assume $\varepsilon_{III} \leq \varepsilon_{II} \leq \varepsilon_I$ in the following derivation. Therefore, the above equivalent strain reduces to

$$F_T^0(\varepsilon_{ij}) = Max\{\varepsilon_I - \varepsilon_{II},\ \varepsilon_{II} - \varepsilon_{III},\ \varepsilon_I - \varepsilon_{III}\} = \varepsilon_I - \varepsilon_{III} \tag{A2}$$

To account for the volumetric deformation, the following modified Tresca equivalent strain is introduced:

$$F_T(\varepsilon_{ij}) = Max\{a(\varepsilon_I - \varepsilon_{II}) - b(\varepsilon_I + \varepsilon_{II}),\ a(\varepsilon_{II} - \varepsilon_{III}) - b(\varepsilon_{II} + \varepsilon_{III}),\ a(\varepsilon_I - \varepsilon_{III}) - b(\varepsilon_I + \varepsilon_{III}),\ e\varepsilon_I\} \tag{A3}$$

where *a*, *b*, and *e* are material parameters. The strain failure criterion associated with F_T is "A material fails if $F_T \geq \varepsilon_C^f$." Among the four competing entities in Eq. A3, the leading three, e.g., $a(\varepsilon_I - \varepsilon_{II}) - b(\varepsilon_I + \varepsilon_{II})$, account for failure due to combined maximum shear and contraction (or dilatation) on the principal planes, while the last one, $e\varepsilon_I$, accounts for maximum stretching failure. We impose $0 < a$ so that the maximum shear strain on a principal plane has a positive contribution to the associated combined failure mode. The inequality $0 < b$ is imposed so as to ensure that a pure and severe enough contraction on any principal plane may cause failure. We also impose $0 < e$ so that the maximum stretching strain (ε_I with a positive value) may cause failure. Note that without the $e\varepsilon_I$ term in Eq. A3, F_T could be negative and the failure surface defined by $F_T(\varepsilon_{ij}) = \varepsilon_C^f$ would not be a closed surface. The condition that the uniaxial compressive strain state $(\varepsilon_I,\ \varepsilon_{II},\ \varepsilon_{III}) = (0,\ 0,\ -\varepsilon_C^f)$ is on the failure surface leads to $a + b = 1$. By using $a + b = 1$ and $\varepsilon_{III} \leq \varepsilon_{II} \leq \varepsilon_I$, we may simplify Eq. A3 to the following:

$$F_T(\varepsilon_{ij}) = Max\{r\varepsilon_I - \varepsilon_{III},\ e\varepsilon_I\} \tag{A4}$$

where $r = a - b$. With the additional parameters, *r* and *e*, we may impose two conditions on the failure surface. Firstly, the pure contraction strain state $(\varepsilon_I,\ \varepsilon_{II},\ \varepsilon_{III})$ = (-100%, -100%, -100%) is on the failure surface. Therefore,

$$Max\{-r + 1,\ -e\} = -r + 1 = \varepsilon_C^f \tag{A5}$$

from which we may infer $0 \leq r < 1$. Secondly, the pure expansion strain state $(\varepsilon_I,\ \varepsilon_{II},\ \varepsilon_{III}) = (\varepsilon_I^f,\ \varepsilon_I^f,\ \varepsilon_I^f)$ is also on the failure surface, where $0 < \varepsilon_I^f$ is the maximum stretching failure strain. Therefore,

$$Max\{(r-1)\varepsilon_I^f,\ e\varepsilon_I^f\} = e\varepsilon_I^f = \varepsilon_C^f \tag{A6}$$

Once values of ε_C^f and ε_I^f are specified, satisfying $0 < \varepsilon_C^f \le 100\%$ and $0 < \varepsilon_I^f$, one can easily calculate *r* and *e* by using Eqs. A5 and A6. One may infer from Eqs. A4 and A6 that a material cannot survive a maximum principal strain greater than or equal to ε_I^f. An alternative approach is to use the uniaxial tensile failure strain, ε_T^f, instead of the magnitude of the uniaxial compressive failure strain, ε_C^f. Note that ε_T^f and ε_I^f satisfy $0 < \varepsilon_T^f \le \varepsilon_I^f$. To implement the alternative approach, we postulate that the uniaxial tensile failure is a combined failure mode, namely,

$$Max\{r\varepsilon_T^f,\ e\varepsilon_T^f\} = r\varepsilon_T^f = \varepsilon_C^f \tag{A7}$$

Substituting Eq. A7 into Eq. A5, one may derive the following:

$$r = 1/(\varepsilon_T^f + 1) \tag{A8}$$

Substituting Eq. A7 into Eqs. A6, one may derive the following:

$$e = r\varepsilon_T^f / \varepsilon_I^f \tag{A9}$$

Therefore, once values of ε_T^f and ε_I^f are specified, satisfying $0 < \varepsilon_T^f \le \varepsilon_I^f$, one can easily calculate *r* and *e* by using Eqs. A8 and A9. The failure surface and material parameters are illustrated by Fig. A1. The figure helps one determine *r* and *e* in a straightforward manner.

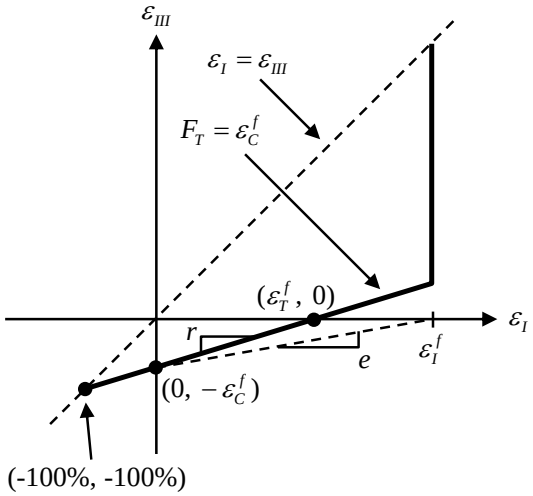

Figure A1. Failure surface, based on the modified Tresca equivalent strain, and the associated material parameters.

The postulate that the uniaxial tensile failure is a combined failure mode reflects a general observation that unsuitability of a mesh cell caused by uniaxial staining is an effect of the distortion or aspect ratio in addition to the cell size. On this postulate, determination of the parameter *r* substantially depends on how one perceives equivalence of the uniaxial tensile failure strain state, i.e., $(\varepsilon_I,\ \varepsilon_{II},\ \varepsilon_{III}) =$

(ε_T^f, 0, 0), and the pure contraction failure strain state, i.e., (ε_I, ε_{II}, ε_{III}) = (-100%, -100%, -100%). For example, if one considers (ε_I, ε_{II}, ε_{III}) = (300%, 0, 0) as undesirable a state of strain failure as (ε_I, ε_{II}, ε_{III}) = (-100%, -100%, -100%), then *r*, which can be calculated with Eq. A8 and is indicated as a slope in Fig. A1, is equal to 0.25. With the decided values of ε_T^f and *r*, one may proceed to select a value of ε_I^f in order to calculate the parameter *e* with Eq. A9. For example, if $\varepsilon_T^f = 300\%$ is chosen, one may choose $\varepsilon_I^f = 750\%$. The selected values result in $e = 0.1$.